CrossMark

Enhanced Visualization and Autonomous Extraction of Poincaré Map Topology

**Wayne Schlei[1] · Kathleen C. Howell[1] ·
Xavier Tricoche[2] · Christoph Garth[3]**

Abstract Poincaré maps supply vital descriptions of dynamical behavior in spacecraft trajectory analysis, but the puncture plot, the standard display method for maps, typically requires significant external effort to extract topology. This investigation presents adaptations of topology-based methods to compute map structures in multi-body dynamical environments. In particular, a scalar field visualization technique enhances the contrast between quasi-periodic and chaotic regimes. Also, an autonomous method is outlined to extract map topology in the planar circular restricted three-body problem. The resulting topological skeleton supplies a network of design options through the interconnectivity of orbital structures.

✉ Wayne Schlei
   wschlei@purdue.edu

   Kathleen C. Howell
   howell@purdue.edu

   Xavier Tricoche
   xmt@purdue.edu

   Christoph Garth
   garth@cs.uni-kl.de

[1]   Armstrong Hall, Purdue University, 701 West Stadium Avenue, West Lafayette,
      IN 47907-2045, USA

[2]   Lawson Hall, Purdue University, 305 N University Street, West Lafayette, IN 47907-2045, USA

[3]   University of Kaiserslautern, PO Box 3049, Kaiserslautern, 67653, Germany

Introduction

The *Poincaré map*, or first-return map, is a powerful tool for analyzing a complex dynamical system. Within the context of multi-body astrodynamics applications, the Poincaré map supplies insight that is otherwise difficult to achieve. Researchers have demonstrated that maps are an effective technique for describing and analyzing capture and escape dynamics of small bodies or spacecraft in the vicinity of moons in three-body models [9, 22]. Another likely benefit in trajectory design scenarios is the identification of low-cost trajectories. Invariant manifolds, a key element in Poincaré map topology, frequently exist as near-optimal options for maneuvering into and out of periodic orbits [12, 21]. Utilizing the invariant manifolds present on a Poincaré map also allows a trajectory designer to construct flyby sequences to transition resonances [1] and initiate strategies to design low-cost transfers between a variety of libration point orbital structures [7, 20]. Considering these potential applications, it is the Poincaré map topology, or the interconnectivity of map components, that frequently supplies the key pieces for effective design strategies in a dynamical system of interest.

Although the Poincaré map provides many benefits and valuable dynamical descriptions, the standard computational methods for generating maps possess several drawbacks. Commonly regarded as the standard approach for displaying Poincaré maps and the associated topology in multi-body gravity models, the *puncture plot* is a representation of the Poincaré map as points indicating the trajectory returns to (or punctures of) a surface of section. These returns are revealed by numerically simulating a set of initial states for a substantial duration and detecting the location of the crossing point on a particular surface of section. For an adequate description of the dynamical behavior on the map, the puncture plot approach requires the solution to numerous initial value problems (i.e., numerical simulations). The resulting point-set visualization of the Poincaré map conveys the general distinction between quasi-periodic regions and chaos; however, visualizing the topological construct that is present in the puncture plot is only attained through significant post-processing analysis. Even locating the periodic orbits in a given map may entail an iterative user-input process without the guarantee of determining structures of relevance to a particular design.

Methodologies employing topology for analyzing scalar fields, vector fields, and dynamical systems are a prevalent research topic in the scientific visualization community. Many vector field visualization methods exploit flow topology to assist in computing important flow structures, and the concepts employed by these methods are also applicable to Poincaré maps. One such example is a software package developed by Yip that combines geometric and graph theory criteria to automatically recognize topological structures in maps defined by analytical expressions [23]. Also, Sanderson et al. describe an approach to connect points in a puncture plot that reside on the same quasi-periodic tori to assist in the approximation of periodic orbits on

the Poincaré map [14]. Finally, Tricoche et al. present a robust and computationally efficient algorithm for extracting topological structure from Poincaré sections in area-preserving Hamiltonian systems with periodic domains involving examples in the Chirikov-Taylor Map (or Standard Map) as well as maps that model plasma confinement in the Tokamak fusion reactor [19]. The study by Tricoche et al. demonstrates that a Poincaré map computation over a relatively sparse grid is sufficient information to extract topological features in a Poincaré section without significant user input [19].

The current investigation attempts to counter the shortcomings of the standard puncture plot approach in generating Poincaré maps for multi-body analysis by adapting topology-based methods. The concepts and algorithm from Tricoche et al. [19] are continued with a focus on astrodynamics applications,revamping the algorithmic details to accommodate the sensitive dynamics that frequently exist in multi-body gravitational models. Specifically, an autonomous Poincaré map topology extraction approach is detailed to assist trajectory analysis and design in the planar circular restricted three-body problem (CR3BP). The contrast between dynamical behaviors associated with a Poincaré section is amplified with a scalar field visualization. The resulting topological skeleton supplies a network of design options through the interconnectivity of various orbital structures. Then, applying this automated topology extraction method inside a visual environment opens an extension of the analysis to interactive design scenarios.

Background

In a time-invariant, Hamiltonian system with two degrees of freedom such as the planar CR3BP, topological structures on Poincaré maps are confined to prescribed itineraries. Let Σ represent a hyperplane that is transverse to the dynamical flow of a near-integrable Hamiltonian system with two degrees of freedom (x, y). The term "near-integrable" refers to a system lacking a full set of integrals of the motion[11]. If the state vector $\boldsymbol{x}_0 = [x, y, \dot{x}, \dot{y}]^T$ (with $\dot{a}$ denoting the time derivative $\frac{da}{dt}$) is located on Σ as indicated in Fig. 1a, then the Poincaré map, or the first-return map, is defined as the mapping

$$\boldsymbol{\mathcal{P}}(\boldsymbol{x}_0) := \boldsymbol{x}_0 \longmapsto \boldsymbol{\mathcal{P}}_\Sigma(\boldsymbol{x}_0), \tag{1}$$

where $\boldsymbol{\mathcal{P}}_\Sigma(\boldsymbol{x}_0)$ represents the first crossing of Σ by the trajectory instantiated by the state $\boldsymbol{x}_0$ through the traversal of a dynamical flow field. Multiple iterates of the Poincaré map are then computed by compounding the first return map, i.e.,

$$\boldsymbol{\mathcal{P}}^p(\boldsymbol{x}_0) = \boldsymbol{\mathcal{P}}_\Sigma(\boldsymbol{\mathcal{P}}_\Sigma(\ldots \boldsymbol{\mathcal{P}}_\Sigma(\boldsymbol{x}_0))), \tag{2}$$

where the map is evaluated for p returns to Σ. Both the initial state and first return to Σ appear as punctures of the green hyperplane in Fig. 1a.

(a) A Poincaré map   (b) Schematic of Poincaré map topology
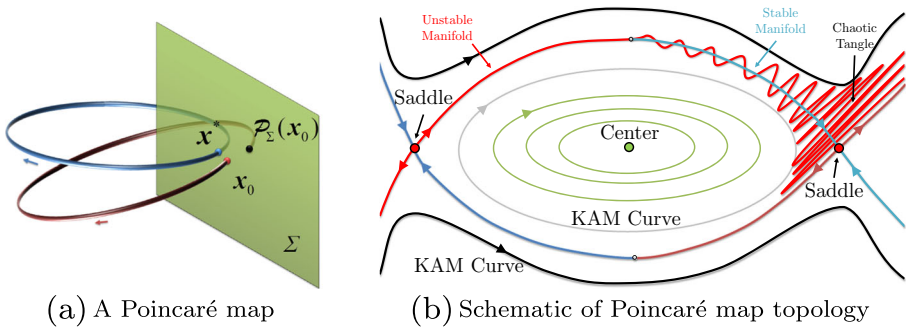
Fig. 1 Available topological structure associated with a Poincaré map in a near-integrable dynamical system[8, 11, 19]

General Behavior

The expected behavior on a Poincaré map for a near-integrable system is classified into three arch-types–periodicity, quasi-periodicity, and chaos[8, 11, 17]. Visible in Fig. 1a, a periodic state, x^*, returns to the same state through the Poincaré map, i.e.,

$$\mathcal{P}^p(x^*) = x^*, \tag{3}$$

where p represents the number of returns required for a p-periodic trajectory to complete an orbit. Such periodic states on the surface of section are named *fixed points* since these points remain fixed when observing the Poincaré map. Fixed points are classified by linear stability analysis as either a center-type orbit with nearby rotational behavior or a saddle-type orbit with hyperbolic attraction and repulsion [8, 11].

The topology available on a Poincaré map emanates from the fixed points that may exist in a region of interest. A plausible schematic topological skeleton of a Poincaré map with saddle-type and center-type behaviors is displayed in Fig. 1b. Quasi-periodic structures exist as closed curves on the Poincaré section that encircle the centers [8, 11]. From Kolmogoroff-Arnold-Moser (KAM) theory, a bounding trajectory, or KAM curve on the map (Fig. 1b), signifies the transition from quasi-periodic behavior to chaotic behavior [11]. Stable and unstable manifolds emerge from the saddle points indicating dynamical flow into and out of saddle-type periodic orbits, respectively [8, 11]. A pivotal element of map topology, especially for low maneuver-cost trajectory design problems, is the connection between saddle points via the unstable-to-stable manifold transition. The stable and unstable manifolds generally intersect an infinite number of due to the chaotic tangles (the driving force of chaos) as seen in Fig. 1b, thereby making manifold tracking difficult [11, 19].

For integrable and near-integrable Hamiltonian systems with two-degrees of freedom, considering the flow along a standard torus (or two-torus) provides an abstract interpretation of the dynamical behavior. Dynamical motion on a torus is described by the uncoupled evolution along two circles tracing out a trajectory on the outer surface [17]. The first circle, defined by the angle θ_1, indicates the cross-sectional evolution along the shorter poloidal dimension whereas the second circle, prescribed

by the angle θ_2, represents motion along the toroidal dimension. The evolutionary history of the poloidal and toroidal angles can be plotted on a square with periodic boundary conditions such as the example appearing in Fig. 2a. The motion along the torus is then characterized by the ratio of the evolutionary frequencies of these two angles, namely,

$$w = \frac{\omega_1}{\omega_2}, \tag{4}$$

where ω_1 and ω_2 are the poloidal and toroidal frequencies, respectively. The quantity w is titled the *winding number* and represents a classification for a particular trajectory. The slope of the angular history chart in Fig. 2a is simply the reciprocal of w as defined in Eq. 4 [11, 17]. Winding numbers with exact integer ratios correspond to periodic orbits. When employing an integer number of rotations, the winding number, w, is defined as the number of poloidal rotations (q) versus the number of toroidal rotations (p), or $w = \frac{q}{p}$. Two sample periodic orbits with winding numbers $w = \frac{1}{1}$ and $w = \frac{3}{2}$ are displayed in Fig. 2a as green and blue trajectories, respectively. The $w = \frac{1}{1}$ orbit (green) completes a poloidal rotation for every toroidal rotation whereas the $w = \frac{3}{2}$ orbit (blue) requires 2 toroidal rotations to complete 3 poloidal rotations, indicated by the different slope in Fig. 2a. In contrast to periodic

(a) Angle History

(b) $w = \frac{1}{1}$ Fixed Point   (c) $w = \frac{3}{2}$ Fixed Point   (d) $w = \frac{\pi}{1}$ Quasi-periodic
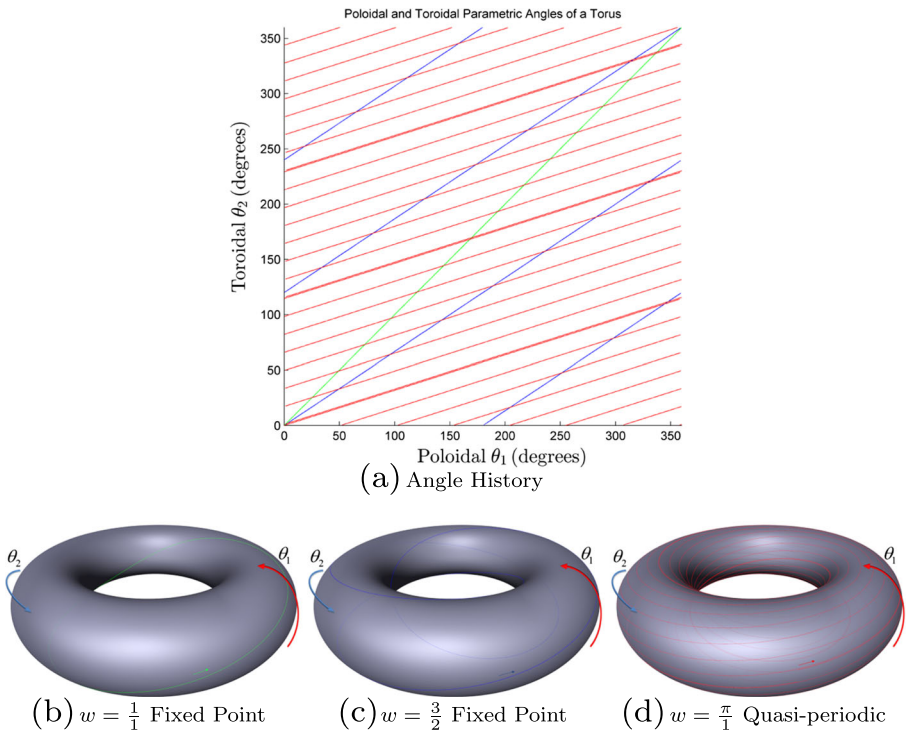
Fig. 2 Dynamical behavior of motion along a torus for a $w = \frac{1}{1}$ orbit (*green*), a $w = \frac{3}{2}$ orbit (*blue*), and a $w = \frac{\pi}{1}$ quasi-periodic trajectory (*red*) [11, 17]

orbits, quasi-periodic trajectories possess irrational winding numbers. Thus, a quasi-periodic orbit such as the $w = \frac{\pi}{1}$ example (red in Fig. 2a) will never trace exactly the same path along the torus but will visit a dense portion of the torus as the trajectory evolves [17]. Near-integrable systems may also include chaos, creating structures that no longer map directly to a torus-type structure [11]. The winding number is, therefore, undefined for chaotic trajectories, but the saddle-type orbits that typically reside within the chaos still possess a valid winding number [11].

Topology Extraction with Puncture Plots

In the planar CR3BP, the standard puncture plot approach renders a Poincaré map as a general depiction and supplies insight into the associated topology. As a sample pair of Poincaré sections, Poincaré maps are computed for the hyperplane $\Sigma : y = 0$ in different systems and displayed as puncture plots in Fig. 3. Domains of interest in the Jupiter-Europa and Earth-Moon systems are selected arbitrarily as

$$D_{JE} = \{(x, \dot{x}) | x \in [-1.5, -1.0], \dot{x} \in [-0.5, 0.5]\}, \tag{5}$$

$$D_{EM} = \{(x, \dot{x}) | x \in [-0.4, 1.1], \dot{x} \in [-2.5, 2.5]\}, \tag{6}$$

respectively, where the range in x and $\dot{x}$ are expressed in nondimensional coordinates. The gravitational parameters (μ) associated with the planar CR3BP are set as $\mu_{JE} = 2.52801770464 \times 10^{-5}$ in the Jupiter-Europa system and $\mu_{EM} = 1.21505714306 \times 10^{-2}$ in the Earth-Moon system. A full state on Σ is then determined by selecting a Jacobi constant (C) value for analysis. For the puncture plots in Fig. 3, initial states are selected randomly throughout the domain and numerically simulated for 200 returns to the surface of section. Each initial state is assigned a unique color, and all subsequent returns from the same initial state are plotted as points with that designated color. Note, the white space bounded by the zero-velocity curves on the section represent the forbidden regions where trajectories are not allowed to evolve due to the Jacobi integral. Quasi-periodic regions are readily visible through the ordered groupings of returns from like-orbits. Trajectories that

(a) Jupiter-Europa ($C = 3.00$)   (b) Earth-Moon ($C = 2.96$)
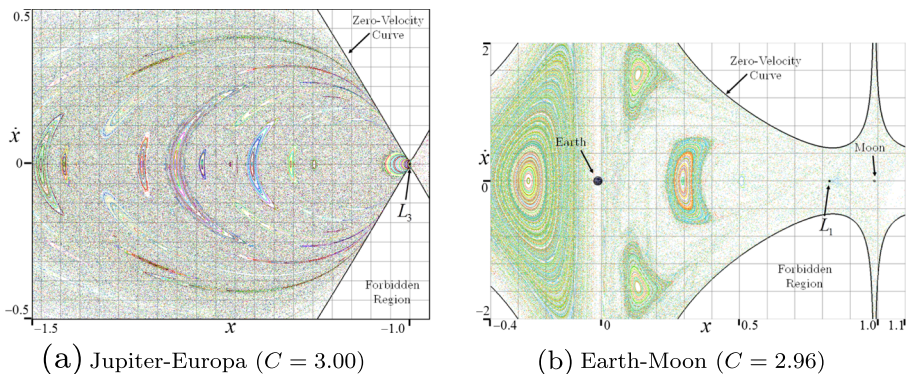
Fig. 3 Sample Poincaré maps for the hyperplane $\Sigma : y = 0$ in the planar CR3BP for different systems and domains visualized with the puncture plot method

reside in chaotic regions appear with unpredictable behavior, and thus, populate a majority of the space where quasi-periodic behavior is not present. Thus, the saddle-type fixed points and the correlated stable and unstable manifolds are difficult to ascertain from the puncture plots in Fig. 3 without additional analysis.

Extracting topology from a puncture plot representation of a Poincaré map involves several steps. Isolation of the topology is initiated by visually locating fixed points in the domain of interest, forming a set of initial guesses for a numerical corrections process. The center-type orbits are easily identified since these fixed points reside in the middle of quasi-periodic regions such as the closed curves in Fig. 3. On the other hand, the hyperbolic saddle points hide in the chaotic sea, i.e., visual acquisition of saddle-type positions is difficult. Alternatively, a designer can locate fixed points that reside on a given Poincaré section by computing families of periodic orbits *a priori* and selecting the orbits that exist at the corresponding Jacobi constant value; however, it is impractical to generate orbit families for *all* the fixed points that appear on a section. Another key component to topology extraction is the computation of the stable and unstable manifolds associated with the saddle-type fixed points. It is standard practice in the puncture plot approach for displaying invariant manifolds on a Poincaré map to generate a set of fixed-points surrounding the periodic orbit and propagate the map for the appropriate perturbations from those states [9, 21]. Unfortunately, this approach produces gaps in the manifold representation due to the divergent behavior of nearby manifold trajectories [1, 20, 21]. This drawback can be mitigated by using a large number of fixed points distributed along the orbit ($> 10^5$ states) with an expensive number of mapping simulations. Overall, Poincaré map topology visualization with the puncture plot method typically requires a significant user effort beyond the initial numerical simulation.

Enhanced Visualization with Orbit Convolution

Although the puncture plot technique offers topological acuity within a system of interest, the *orbit convolution* method is employed for a scalar field depiction of the dynamics associated with a particular Poincaré map [19]. In a manner similar to the *Line Integral Convolution* method for vector field visualization (Cabral and Leedom [2]), the domain of interest for a Poincaré map is overlaid with a colored noise image, $\sigma(\boldsymbol{x})$, such that a random color (σ in RGB color coordinates from [0, 0, 0] to [1, 1, 1]) exists at each pixel (or grid node) in an $N \times M$ image. The Poincaré map is then computed for each node in the image for n returns to the relevant surface of section. The resulting color image for a given initial state, $I(x)$, is then the average color mapping corresponding to the given number of iterations of the Poincaré map, i.e.

$$I(\boldsymbol{x}) = \frac{1}{n} \sum_{p=0}^{n} \sigma(\mathcal{P}^p(\boldsymbol{x})). \tag{7}$$

Here, p is an increasing sequence of map iterates such that $\mathcal{P}^p(\boldsymbol{x})$ is contained in the domain of interest (i.e., there is a corresponding pixel in the input image). The resulting image identifies pixels (i.e., initial states) that reside on the same periodic

or quasi-periodic orbit as a single color since the map corresponding to these states will visit the same set of colors on the noise image. Chaotic trajectories intersect $\sigma(\boldsymbol{x})$ at seemingly random locations due to the unpredictable motion. The orbit convolution procedure reflects the chaotic behavior as a average color value that tends towards the expectation value of the colored noise–gray (or [0.5, 0.5, 0.5] in RGB color coordinates) [19].

Modifications to the original orbit convolution procedure are required to adapt this approach to maps in multi-body regimes. Computing a large number of map iterations for a dense grid of initial states produces sufficient quality in a final visualization but at a high computational expense. A reduction in computational cost is achieved by replacing a large total number of orbit intersections, n, with extra convolution passes, thereby reducing the total number of numerical integrations. Let K represent the number of convolution passes applied to $I(\boldsymbol{x})$. If a convolution pass (Eq. 7) is expressed in terms of an operator $\mathcal{W}$, successive convolution passes generate the resulting image

$$I(\boldsymbol{x}) = \mathcal{W}^K(\boldsymbol{x}), \tag{8}$$

where the result of one convolution pass $(K-1)$ is used as the input to the subsequent pass (K), beginning with a noise image in the first pass $(K = 1)$. Essentially, the extended convolution is independent of the numerical propagation and, thus, trajectories are pre-computed and retained in memory for use in each subsequent convolution pass. A high-pass image filter is also employed after each convolution pass to preserve the contrast between available structures[19]. If the orbit convolution image is utilized as a rough background skeleton for the topology of the Poincaré map, the computational cost can be further mitigated by using a lower-accuracy simulation (numerical simulation with a higher error tolerance). In multi-body dynamical models, some initial states residing in an arbitrarily chosen sampling domain may reside within regions of non-real dynamical behavior (e.g., the forbidden regions in the CR3BP). It is also possible for a spacecraft trajectory to depart the primary system (i.e., the domain of interest) or for numerical sensitivities to impede the simulation of a particular initial state. Thus, a sufficient number of hyperplane intersections (n) cannot be reliably computed for some pixels. When such an event occurs, the corresponding pixels in orbit convolution images are marked as white pixels.

When applied to planar CR3BP examples, the orbit convolution method creates images with an evident distinction between quasi-periodicity and chaos. The orbit convolution scalar field for a 512×512 grid representing the domain D_{JE} in the Jupiter-Europa system is illustrated in Fig. 4 with $n = 100$ returns and different degrees of convolution passes. The white areas in Fig. 4 embody the forbidden regions in the dynamical flow for D_{JE}. The resulting image in Fig. 4a demonstrates the result of applying the color blending identified in Eq. 7 (i.e., a solitary convolution pass). Two additional convolution passes with high-pass filtering are applied to the same set of data for enhanced clarity (Fig. 4b). The resulting image efficacy is dramatically improved by utilizing multiple convolution passes even though the number of map iterates is unchanged. The gray regions in Fig. 4b represent the state locations in D_{JE} that

(a) $K = 1$ (b) $K = 3$
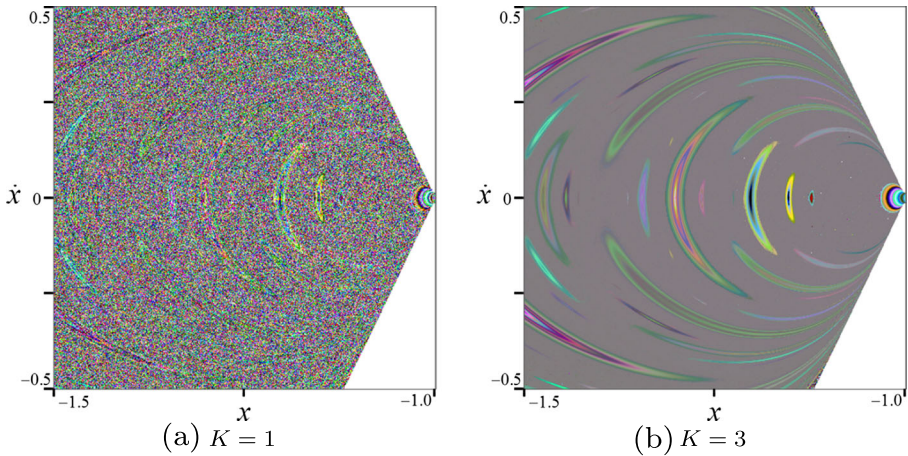
Fig. 4 Orbit convolution visualization technique applied to a Poincaré section in the Jupiter-Europa system with parameters $n = 100$ iterates and K convolution passes

exhibit chaotic behavior as the map is propagated forward. Quasi-periodic trajectories appear in regions possessing the same non-gray color. Since the color values are randomly generated from the noise image, two distinct and separate orbital structures may display very similar colors. Fortunately, it is easy to disassociate like-colored structures as the color pattern in a given island chain remains consistent.

Orbit convolution reveals additional Poincaré map behavior in an example formulated in the Earth-Moon system. A visualization of the domain D_{EM} is portrayed in Fig. 5 as a 1024×512 grid with $K = 3$ convolution passes. The resulting image again conveys chaotic regions in gray and regions of ordered behavior with a non-gray color. In contrast to the Jupiter-Europa example, large areas of the domain of interest in Fig. 5 do not yield a sufficient number of map iterates in practical time, leading to
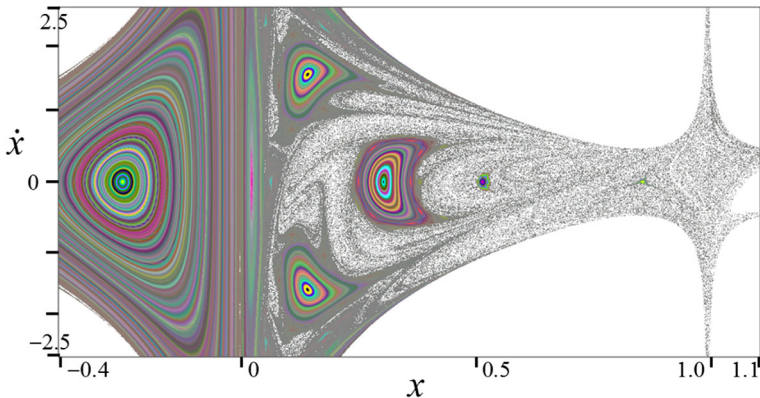
Fig. 5 Orbit convolution visualization technique applied to a Poincaré section in the Earth-Moon system with parameters $n = 100$ iterates and $K = 3$ convolution passes

a large number of white pixels between viable regions; however, these white-tagged trajectories are still a part of the chaos, and in fact, display the tendency to depart the Earth-Moon vicinity (i.e., the evolution of the simulated path does not return to the domain of interest).

Autonomous Topology Extraction

Employing an algorithm for autonomous topology extraction generates the pertinent topological features of a Poincaré map (i.e., periodic orbits and applicable invariant manifolds) with minimal user input. The details of automated topology extraction from a Poincaré map for a domain of interest are established by Tricoche et al. [19], but adaptations to multi-body dynamical environments are the current focus of this investigation. The procedure for extracting topology relies on the user for an initial definition of the Poincaré section and the domain of interest. The resulting orbital structure, though, is generated through an automated orbit-detection technique that is designed to utilize parallel processing while minimizing the overall performance bottlenecks.

Numerical Propagation Scheme Selection

Minimizing map iteration compute times is achieved by assigning the appropriate numerical propagation technique to a suitable task. The most time-consuming numerical procedure for developing the Poincaré map is evaluating the Poincaré map itself through simulation and root-solving. Runge-Kutta methods with adaptive error control are preferable over predictor-corrector methods when computing a Poincaré map since Runge-Kutta methods automatically generate an interpolating polynomial between subsequent steps, rendering root-finding as a simple step [13]. The current investigation implements a Dormand-Prince fifth-order method for computing maps and the fixed point detection procedure. Assuming that the bottleneck for computation time is executing a map iteration, elements of the automated topology extraction process are tailored to minimize the total number of required mappings as well as enhance the speed of each Poincaré map computation where possible. In some phases of topology extraction, it is more desirable to form a general depiction of the behavior quickly rather than extreme accuracy; in these general behavior computations, including the orbit convolution procedure or the initial grid sampling, the error tolerances on the Dormand-Prince method are elevated to 1×10^{-8} for enhanced speed. Where more precision is needed (e.g., refining a fixed point or computing a manifold), an error tolerance of 1×10^{-12} supplies the required accuracy.

Poincaré Section Definition and Initial Sampling

Implementation of the autonomous extraction strategy initially requires isolation of a hyperplane and a sampling grid to represent the domain of interest. The surface of section, Σ, is essential to all phases of the process and must be declared as a first step to initiate the process. In this investigation, the hyperplane $\Sigma : y = 0$ is employed

exclusively, but other hyperplanes are permissible and may be more suitable for other applications. The sampling grid can possess a rather low resolution (e.g., 16×16 or 20×20); note, however, that the number of resulting orbital structures is increased as the sampling resolution increases since the Poincaré map possesses a fractal nature [19]. Orbit convolution imagery offers valuable insight into selecting a domain of interest since the contrast between possible structures is already highlighted. Thus, topology extraction can be focused on key regions identified by orbit convolution. Poincaré maps possess fractal properties, meaning more information appears as a region of interest is narrowed [11]. Therefore, a specified maximum on the number of toroidal periods (p_{max}) confines the search for topological structures to a practical level [19]. At each node of the user-specified sampling grid, the Poincaré map is numerically simulated in parallel utilizing error tolerances that favor a general description of dynamical behavior over high accuracy (i.e., computational speed is increased by employing 1×10^{-8} versus 1×10^{-12}). The numerical simulation is executed for a relatively long duration such that the total number of map iterates, n, is sufficiently large for an accurate representation of the space ($n \in [100, 200]$ is usually sufficient in the current work).

Node Trajectory Classification

A general sense of dynamical behavior is achieved by designating a corresponding scalar quantity at each grid node. Essentially, the classification phase determines the scalar metric as the available toroidal periods for a particular location. Classifying the behavior at each grid node allows the algorithm to operate over a smaller subset of toroidal periods rather than the entire range $[1, p_{max}]$. The subsequent steps in the automated topology extraction algorithm are comprised of operations on grid cells that collect the available toroidal periods at each grid node to run mapping computations. Reducing the operational range on the toroidal period translates to enhanced efficiency since p values that are not associated with a cell are skipped.

In an area-preserving (2D) Hamiltonian system, a good choice for a classifying parameter is the winding number since this parameter suggests a fundamental dynamical behavior and a toroidal period [11, 19]. Since the planar CR3BP is a time-invariant Hamiltonian system, periodic and quasi-periodic regions on the surface of section are confined to a two-torus and, hence, are fully described by a single winding number [7, 8, 11, 17]. Numerically evaluating this winding number requires a transformation from state space to a more appropriate set of coordinates (e.g., action-angle variables)–an excessively complex procedure for a algorithm seeking an efficient execution. As an alternative, Lichtenberg and Liebermann demonstrate that multiple winding numbers exist for Hamiltonian systems of higher dimension ($N \geq 3$) [11]. Although the planar CR3BP is a 2D Hamiltonian system, Cartesian position and velocity coordinates expressed in terms of a rotating reference frame are typically employed as the variables for dynamical modeling. Thus, a collection of winding numbers is produced utilizing only the state space coordinates to isolate plausible toroidal periods for an individual node on the grid. The computation of this collection of winding numbers is accomplished congruently with the numerical simulation via the tracking of particular angles as they rotate about the origin (i.e., the

barycenter in the planar CR3BP). An angle of rotation, θ_{ab}, for Cartesian coordinates a and b is measured as the cumulative rotation that the 2D vector $r_{ab}(t) = [a_t, b_t]^T$ traces during the numerical simulation process with the current time step indicated by t; this rotation angle is then defined as the signed angle

$$\theta_{ab} = \sum_{t=0}^{t_n} \arccos \left(\frac{r_{ab}(t + \Delta t) \cdot r_{ab}(t)}{\|r_{ab}(t + \Delta t)\| \|r_{ab}(t)\|} \right), \tag{9}$$

where t_n reflects the total simulation time to achieve n map iterates and Δt represents the current step size in the differential equation solver. By convention, a value such that $\theta_{ab} > 0$ identifies counter-clockwise rotations about the origin. The suitable state space coordinate combinations include x, $\dot{x}$, and $\dot{y}$, yet naturally exclude the defining coordinate of the hyperplane (y). The set of available winding numbers is then $W = (w_{x\dot{x}}, w_{x\dot{y}}, w_{\dot{x}\dot{y}})$, where the individual ratios are computed as

$$w_{x\dot{x}} = \frac{2\pi n}{\theta_{x\dot{x}}}, w_{x\dot{y}} = \frac{2\pi n}{\theta_{x\dot{y}}}, w_{\dot{x}\dot{y}} = \frac{2\pi n}{\theta_{\dot{x}\dot{y}}}. \tag{10}$$

Fortunately, these rotation angles are tracked concurrently during the initial map simulation and without noticeable penalty to computational efficiency. The approximation of the winding numbers converge to the true value as $n \to \infty$ [19], but the initial sampling reaches a suitable approximation for the winding numbers within the prescribed range for n.

Classification via winding number is conveyed through the combination of puncture plots and scalar field visualizations. As an example, the computed set W is displayed as colored scalar fields mapped to a puncture plot originating from a randomly seeded set of initial states within the domain D_{EM} (Fig. 6). Examining Fig. 6a, most trajectories (periodic, quasi-periodic, and chaotic) hold a winding number with the value $w_{x\dot{x}} = \frac{-1}{1}$ (indicated by the greenish color), even though the orbital behavior varies significantly throughout the domain. The prevalence of the same characteristic number throughout the Poincaré section in Fig. 6a is clear evidence that more than one winding number is necessary to classify which toroidal periods are representative of an arbitrary initial state. The $w_{x\dot{y}}$ number, appearing in Fig. 6b, supplies a strong contrast between quasi-periodic behavior (residing at the white and yellow extrema of the indicated color map) and chaotic behavior which transitions through the purple range near $w_{x\dot{y}} = 0$. The final winding number, $w_{\dot{x}\dot{y}}$ as displayed in Fig. 6c, completes the classification of a grid node. The appearance of $w_{\dot{x}\dot{y}}$ in Fig. 6c is similar to the winding number $w_{x\dot{x}}$ (Fig. 6a), but ratios within the $w_{\dot{x}\dot{y}}$ field are set apart from the $w_{x\dot{x}}$ field, meaning additional information is acquired. Although the winding number associated with chaotic initial states is undefined, motion along chaotic trajectories is influenced by nearby saddle-type fixed points. As a result, the winding numbers corresponding to chaotic initial states computed through rotation-tracking yield a classification of nearby behavior even though a "true" winding number does not exist.

Generating the classification of toroidal periods per grid node requires a conversion from the set W to a set of plausible integers that indicate the representative
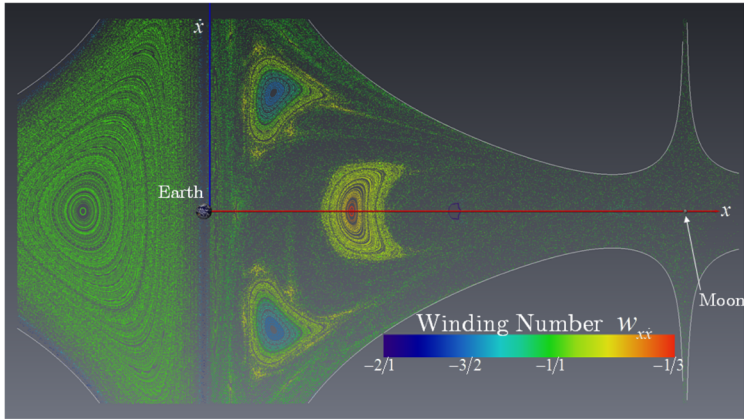
(a) $w_{x\dot{x}}$
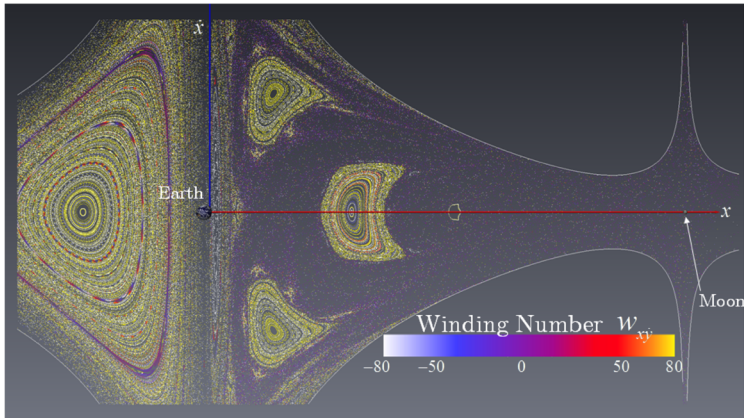
(b) $w_{x\dot{y}}$
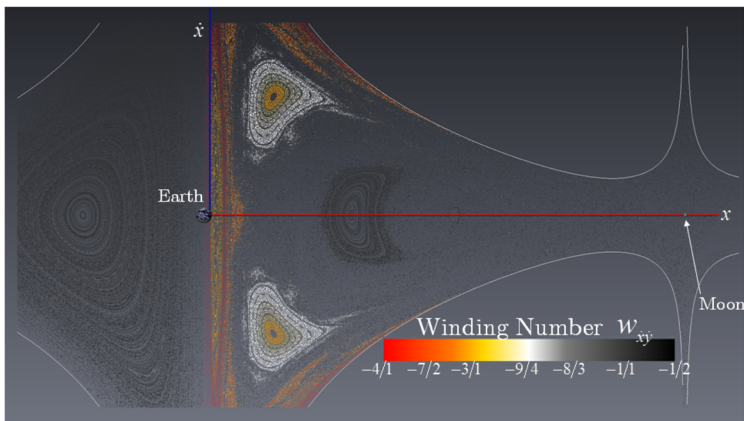
(c) $w_{\dot{x}\dot{y}}$

Fig. 6 Classification of the space using winding numbers; the Earth-Moon system domain D_{EM} computed for a set of randomly seeded initial states ($n = 200$)

number of Poincaré map iterates. The winding number is often represented as a *continued fraction*, or

$$w = a_0 + 1/(a_1 + 1/(a_2 + 1/(a_3 + \ldots, \tag{11}$$

where the coefficients, a_j, are selected to approximate w to a specified precision [16, 19]. Computing the excited toroidal periods at a grid node from W involves converting each winding number to the nearest integer ratio. A continued fraction algorithm (such as the methodology by Shoemake [16] and Thrill [18]) is employed to compute the best rational approximation for each winding number at every grid node. This algorithm identifies the best integer ratio approximation where the highest allowable denominator is equal to p_{max}. The denominator in each winding number integer ratio represents a possible toroidal period for a fixed point within a nearby grid cell. As asample scenario for computing toroidal periods, consider a 24×16 sampling grid mapped to the domain D_{EM} with $p_{max} = 12$. The resulting grid, as well as the set of plausible toroidal periods from the continued fraction algorithm, are displayed in Fig. 7. The continued fraction algorithm yields 3 integer values at each grid node that classify the potential toroidal periods at nearby fixed points. An example set of potential toroidal periods is indicated in Fig. 7 as the red highlighted set [1 11 1]; the 3 values indicated in the highlighted set ([1 11 1]) correspond to the denominator of each approximate integer ratio as the continued fraction algorithm is applied to the winding number set W. Thus, the values 1, 11, and 1 represent the toroidal number of rotations for the winding numbers $w_{x\dot{x}}$, $w_{x\dot{y}}$, and $w_{\dot{x}\dot{y}}$, respectively. The influence of nearby fixed points is illustrated by observing grid cells that encircle a period-1 (or $p = 1$) center-type fixed point (appearing within the yellow cells in Fig. 7). Each
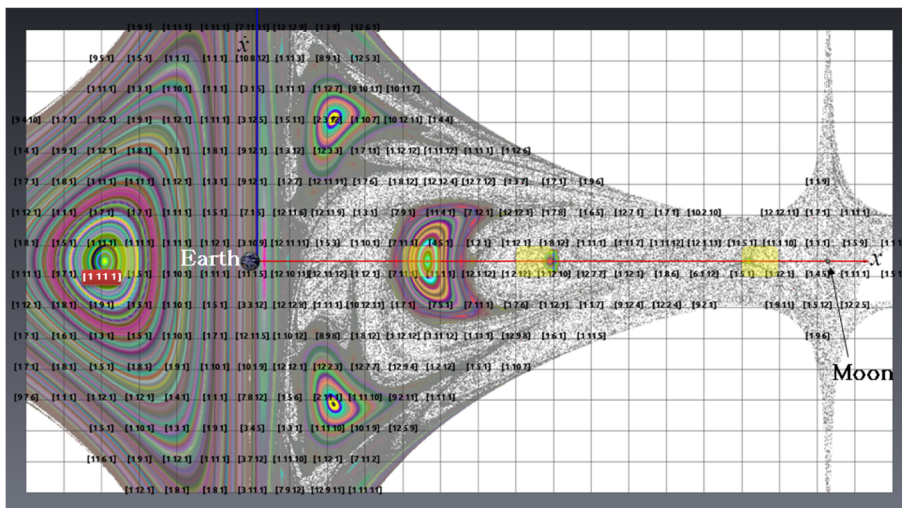
Fig. 7 Available periods for each grid node of a sample grid (24×16) applied to the domain D_{EM} with $p_{max} = 12$. The possible periods are the denominators of the set of winding numbers, W, computed with a continued fraction algorithm

grid node from the yellow cells includes the value $p = 1$ as a member of the plausible set of periods, so the initial states that are close to the period-1 center-type fixed points all demonstrate dynamical behavior that is similar to the nearby center. The automated fixed point detection process examines each cell by searching for fixed points that possess a toroidal number of rotations indicated by the set of plausible toroidal periods available at each corner. Although each cell could examine up to 12 toroidal periods based on 4 grid nodes offering 3 possible values, it is common that integers in the set at a single node are repeated at all of the nodes of cell, and thus, the total number of toroidal periods examined per-cell remains much lower than the full range $[1, p_{max}]$.

Periodic Orbit Detection

The location of fixed points that likely exist within the initial sampling grid is achieved autonomously with an application of index theory. Let Γ represent a closed curve that encircles an isolated fixed point. Also, define the vector $\mathbf{\Delta}$ as a displacement vector between x, an initial state on the surface of section, and the Poincaré map representation of that state to p iterations, or namely

$$\mathbf{\Delta} = \mathcal{P}^p(x) - x. \tag{12}$$

The *Poincaré index* is then defined as the summation of the signed angles of rotation that the vector $\mathbf{\Delta}$ generates over Γ [8]. Let the angle α represent the orientation of $\mathbf{\Delta}$ with respect to the x-axis through the dot product

$$\mathbf{\Delta} \cdot \hat{x} = \|\mathbf{\Delta}\| \cos(\alpha), \tag{13}$$

where α is computed as a function of the current map displacement (or $\alpha(\Delta)$). On the surface of section in the planar CR3BP, the Poincaré index, k, is represented utilizing the coordinates existing on the section through the line integral

$$k = \frac{1}{2\pi} \oint_{\Gamma} d\left(\arctan\left(\frac{d\dot{x}}{dx}\right)\right) = \frac{1}{2\pi} \oint_{\Gamma} d\alpha(\mathbf{\Delta}), \tag{14}$$

with the x and $\dot{x}$ coordinates on the section [8, 19]. If the Poincaré index is non-zero, a fixed-point exists inside the closed-curve Γ, and index values of $k > 0$ and $k < 0$ correspond to center-type and saddle-type fixed points, respectively [8, 17]. The cell edges that comprise the initial sampling grid form the closed-curve on the surface of section within the topology extraction algorithm and, thus, the Poincaré index is evaluated for each possible toroidal period (p) obtained during the node classification process. Along each edge in the sampling grid for a particular p value, the map displacement vector $\mathbf{\Delta}$ is computed in sufficiently small increments such that the rotation of $\mathbf{\Delta}$ (or the change in the angle $\alpha(\mathbf{\Delta})$) exhibits a clear and monotonic transition. The resulting change in α tracked along an edge of a grid cell then contributes a portion of the total integral in Eq. 14. Specifically, the Poincaré index for a cell is then the signed, counter-clockwise summation of these partial edge-rotation contributions computed for all sides of the cell. Grid cells that return a non-zero index for a specified value of p are then processed to generate an initial guess for a fixed point.

Pruning redundant computations during the evaluation of the Poincaré index assists in maintaining algorithmic efficiency. Evaluating the Poincaré index per-cell implicitly generates duplicate computations since some cells share the same edge. Thus, a per-edge computation is employed to enhance the computational speed of the detection process. Each edge is paired with the set of possible toroidal periods that must be evaluated. Then, a rotation angle refinement procedure is executed in parallel. The change in orientation of the vector $\mathbf{\Delta}$ between subsequent points along an edge may exhibit an ambiguity (i.e., the direction of rotation for a 180° transition in α is unclear). The rotation of $\mathbf{\Delta}$ is then computed under a maximum variation cap to avoid ambiguous scenarios (135° is employed in the current work) through adaptive sampling along an edge. The adaptive edge subdivision continues until the angle of rotation is resolved or a minimum distance between consecutive sample points is achieved. Selecting this minimum distance, or d_{min}, is problem-dependent [19]. In a scenario where the rotation in $\mathbf{\Delta}$ is not monotonic or the rotation angle between subsequent points is undetermined, the algorithm labels the index as unavailable and continues to the next process. In cases where adjacent sample points along an edge that are within the distance d_{min} that also indicate an instantaneous flip in $\mathbf{\Delta}$ (or a change in α of 180°) with a small $\|\mathbf{\Delta}\|$, a fixed point may exist in close proximity to the edge. Where the algorithm encounters a rotation ambiguity of $180° \pm 10°$, the state along the edge is saved as a suitable guess for a fixed point to be employed later in a refinement procedure.

Determining an initial guess for a fixed point is a critical step in any map topology extraction procedure. If a guess for a fixed point is too distant from the true location, most periodic orbit targeting procedures struggle to converge. Constructing the initial guess within a grid cell is achieved through one of several possible methods. An exceptionally simple approach utilizes the midpoint of a cell as the guess, but this guess-construction strategy typically generates a poor result for sensitive problems such the planar CR3BP. As an alternative, the approach employed in this work broadens guess generation within a cell via a sub-cell grid search where the algorithm examines the map displacement ($\mathbf{\Delta}$) for the indicated number of iterates for each sub-cell grid state. The sub-grid state with the smallest displacement is then assigned as the initial guess. The sub-grid search involves more computations compared to the midpoint guess since the Poincaré map is processed for many sub-grid nodes; however, this thorough search approach encompasses the nonlinear effects of the problem[19].

Fixed Point Refinement

The fixed points are computed to finer precision utilizing the automated guesses resulting from the detection phase as input. The computation process as described by Tricoche et al.[19] is reinforced with a multiple shooting scheme to accommodate the sensitive dynamics associated with corrections procedures in multi-body problems. In the present work, the differential corrections scheme employs a general multiple shooting algorithm for constructing periodic orbits based on a user-specified arbitrary number of patch points (or fitting points designed to match constraints) that partition a trajectory segment[15].

The multiple shooting algorithm employed in this work first isolates a set of design variables that are iteratively modified to meet constraints that apply to periodic orbits. Definition of the design-variable vector, X, requires the user to specify the number of patch points between successive iterates, m, such that trajectory segments from the simulation of a particular solution step (j) are split into $k = mp$ patch points with $k - 1$ trajectory segments. The state vectors corresponding to the k patch points and the orbital (time) period, T, are collected to form the design-variable vector as

$$X^j = \begin{Bmatrix} x_0^j \\ x_1^j \\ \vdots \\ x_{k-1}^j \\ T^j \end{Bmatrix}, \tag{15}$$

where the dimension of X^j is $Nk + 1$ with N representing the state space dimension ($N = 4$ in the planar CR3BP). Note that the j superscript signifies the current iteration in the differential corrections process. The initial guess vector X^0 is populated with the autonomously detected information in the previous phase (Section 3). The approximated fixed point coordinates $(x, \dot{x})$ for a given p are converted to the initial state x_0^0 employing the hyperplane definition and the Jacobi constant. Then, the evolution of x_0^0 through $\mathcal{P}^p(x_0^0)$ is simulated, setting T as the propagation time at the final crossing of Σ. The remaining $k - 1$ state entries in X^0 are sampled from the propagated evolution at equal time intervals of T/k. An illustration of the segments and patch points for a $p = 1$ analysis appears in Fig. 8. The blue initial guess is a
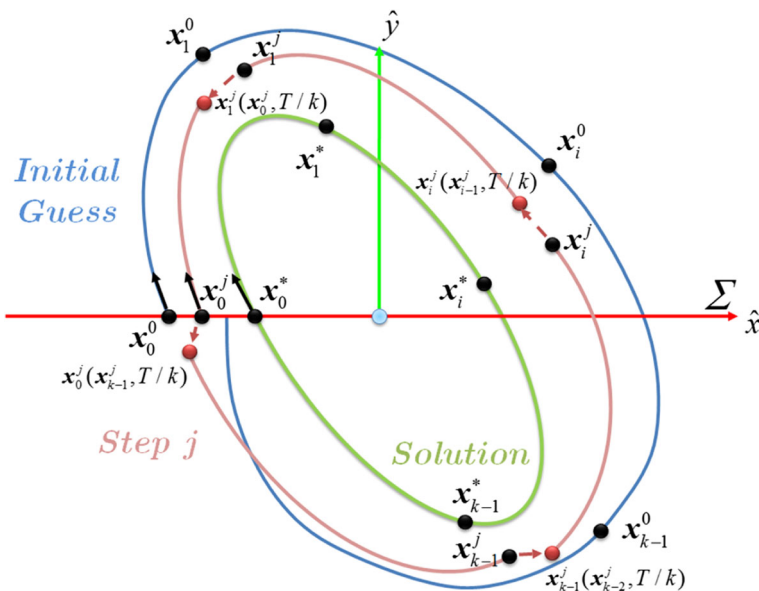
Fig. 8 Schematic diagram of the fixed point refinement procedure employing a multiple shooting approach with k patch points given a $p = 1$ initial guess [15].

continuous evolution with displacement only existing between the initial state and the final return to the section whereas the desired periodic solution (green) is continuous throughout the evolution of $\mathcal{P}^p(\boldsymbol{x}_0^*)$. Intermediate steps in the solution process, such as the red arcs indicating the jth step, may possess discontinuities between patch points, which are highlighted through the numerical simulation of a patch point over a specified time interval. The notation $\boldsymbol{x}_1^j(\boldsymbol{x}_0^j, T/k)$ indicates the final state from the propagation of $\boldsymbol{x}_0^j$ through simulation time T/k. The goal of the solution process is a continuous periodic solution. The superscripts on X^j components (such as $\boldsymbol{x}_0^j$ and T^j) are omitted from component entries henceforth for clarity.

The problem input to the multiple shooting process in autonomous Poincaré map topology extraction is the isolation of the true fixed point location such that conditions for a periodic orbit are satisfied (to an arbitrary tolerance). Such periodic orbit conditions include constraints to enforce continuity between segments. Thus, $N(k-1)$ constraints enforce continuity at the patch points, and $N-1$ constraints ensure the periodicity conditions, i.e., that the propagation of the $k-1$ state for the time period T/k matches the initial state through

$$\tilde{\boldsymbol{x}}_0(\boldsymbol{x}_{k-1}, T/k) - \tilde{\boldsymbol{x}}_0 = 0. \tag{16}$$

Note that $\tilde{\boldsymbol{x}}$ represents a partial state vector where the transverse component of velocity ($\dot{y}$) is excluded. The multiple shooting algorithm employed in the fixed point refinement procedure also restricts that the first state resides on the specified hyperplane, Σ, via the equation representing the section or

$$D_\Sigma(\boldsymbol{x}_0) = y_0 = 0. \tag{17}$$

The initial state is also constrained to possess the specified Jacobi constant value for analysis, or C_D as defined by the user, through the additional constraint equation

$$C(\boldsymbol{x}_0) - C_D = 0, \tag{18}$$

where $C(\boldsymbol{x}_0)$ is simply the Jacobi integral in the planar CR3BP evaluated at the initial state, or

$$C(\boldsymbol{x}) = 2\Upsilon - (\dot{x}^2 + \dot{y}^2), \tag{19}$$

and

$$\Upsilon = \frac{1-\mu}{d} + \frac{\mu}{r} + \tfrac{1}{2}(x^2 + y^2), \tag{20}$$

represents the pseudo-potential function that is strictly position dependent with d and r indicating distances from the larger and smaller primary bodies, respectively [3,

10]. Overall, the constraint vector, $\boldsymbol{F}$, incorporates the patch point continuity constraints and all additional constraints for iteration j in the form

$$\boldsymbol{F}(X^j) = \begin{Bmatrix} \boldsymbol{x}_1(\boldsymbol{x}_0, T/k) - \boldsymbol{x}_1 \\ \boldsymbol{x}_2(\boldsymbol{x}_1, T/k) - \boldsymbol{x}_2 \\ \vdots \\ \boldsymbol{x}_{k-1}(\boldsymbol{x}_{k-2}, T/k) - \boldsymbol{x}_{k-1} \\ \tilde{\boldsymbol{x}}_0(\boldsymbol{x}_{k-1}, T/k) - \tilde{\boldsymbol{x}}_0 \\ D_\Sigma(\boldsymbol{x}_0) \\ C(\boldsymbol{x}_0) - C_D \end{Bmatrix}. \tag{21}$$

Note, the first $N(k-1)$ entries of $\boldsymbol{F}$ represent the continuity conditions applied to the patch points. This formulation yields $\boldsymbol{F}(X^*) = \boldsymbol{0}$ when the periodic solution X^* is attained.

Essentially, the solution process is an iterative root-finding problem, seeking to drive the constraint vector to zero by changing the design variables [13, 15]. Since the formulation employs $Nk + 1$ design variables to uphold $Nk + 1$ constraints, the refinement procedure utilizes the Newtonian update formula for computing the next variable set, X^{j+1}, given the current solution step X^j as

$$X^{j+1} = X^j - D\boldsymbol{F}(X^j)^{-1}\boldsymbol{F}(X^j), \tag{22}$$

noting that $D\boldsymbol{F}(X^j)$ represents the Jacobian matrix of $\boldsymbol{F}(X^j)$ with respect to X^j [13, 15]. A solution is achieved when $\|\boldsymbol{F}(X^j)\| < \epsilon$, where $\epsilon = 10^{-8}$ in the present work. Analytical expressions are available for the Jacobian matrix via

$$D\boldsymbol{F}(X) = \begin{bmatrix} \frac{\partial \boldsymbol{x}_1(\boldsymbol{x}_0, T/k)}{\partial \boldsymbol{x}_0} & -I & & & \frac{\dot{\boldsymbol{x}}_1(\boldsymbol{x}_0, T/k)}{k} \\ & \frac{\partial \boldsymbol{x}_2(\boldsymbol{x}_1, T/k)}{\partial \boldsymbol{x}_1} & -I & & \frac{\dot{\boldsymbol{x}}_2(\boldsymbol{x}_1, T/k)}{k} \\ & & \ddots & \ddots & \vdots \\ & -\tilde{I} & & \frac{\partial \tilde{\boldsymbol{x}}_0(\boldsymbol{x}_{k-1}, T/k)}{\partial \boldsymbol{x}_{k-1}} & \frac{\dot{\tilde{\boldsymbol{x}}}_0(\boldsymbol{x}_{k-1}, T/k)}{k} \\ & \Psi & & & \end{bmatrix}, \tag{23}$$

with $\tilde{I}$ and Ψ representing special submatrices, and the missing entries in the $D\boldsymbol{F}(X)$ matrix are zero elements. Entries in the last column of $D\boldsymbol{F}(X)$ are evaluated as the state derivatives at the end of the specified numerical simulation multiplied by a constant $(1/k)$. For the periodicity condition in Eq. 16, the indicated special submatrix $\tilde{I}$ is a modified identity matrix with the appropriate row removed. The special submartrix represents the analytical derivatives

$$\Psi = \begin{bmatrix} \frac{\partial D_\Sigma(\boldsymbol{x}_0)}{\partial \boldsymbol{x}_0} \\ \frac{\partial C(\boldsymbol{x}_0)}{\partial \boldsymbol{x}_0} \end{bmatrix} = \begin{bmatrix} 0 & 1 & 0 & 0 & 0 & 0 \\ 2\frac{\partial \Upsilon(\boldsymbol{x}_0)}{\partial x_0} & 2\frac{\partial \Upsilon(\boldsymbol{x}_0)}{\partial y_0} & 2\frac{\partial \Upsilon(\boldsymbol{x}_0)}{\partial z_0} & -2\dot{x}_0 & -2\dot{y}_0 & -2\dot{z}_0 \end{bmatrix}, \tag{24}$$

for the remaining constraints on the initial state. To assist with the corrections process, the state transition matrix (STM or $\frac{\partial \boldsymbol{x}_b(\boldsymbol{x}_a, t)}{\partial \boldsymbol{x}_a}$ evaluated from $\boldsymbol{x}_a$ to $\boldsymbol{x}_b$ through time t) is propagated concurrently with any given state vector and supplies continuity derivatives between individual fitting points [15].

After the initial guesses are refined to periodic orbits, the resulting fixed points are classified and filtered. The full-period STM (or monodromy matrix) is employed to classify the orbital stability characteristics through the standard eigenvalue analysis [8, 21]. If λ represents the monodromy matrix eigenvalue with maximum magnitude, then a periodic orbit with $|\lambda| > 1$ is classified as a saddle-type fixed point [8]. All other computed fixed points are classified as centers. Duplicate fixed points may appear as a result of the extraction process, especially higher period duplicates of the same periodic orbit; fixed points representing duplicates are filtered by retaining only the lower-period version of a duplicated set. Many asymmetric periodic orbits exist in the planar CR3BP, but both pairs of asymmetric orbits (via the symmetry properties of the CR3BP) may not always be located through the detection or refinement phases. The filtering process, therefore, should also include the evaluation of symmetric counterparts to any identified orbits.

Manifold Extraction

For the saddle-type fixed points, the stable and unstable manifolds are computed in the final stage of the algorithm. Here, manifolds are located employing an alternative approach to the puncture plot method, one that is suited for a Poincaré section (namely, a 1D continuation scheme offered by England et al. [6]). This technique constructs manifolds exclusively on the Poincaré section by solving a successive sequence of shooting problems. After initializing the method with a vector perturbation, δx, from a fixed point, x^*, along the appropriate direction associated with the eigenvector from the monodromy matrix, an upstream interval, $[x^*, x^* + \delta x]$, is established. Assuming this interval approximates a linear segment along the manifold, states along the upstream interval are mapped via $\mathcal{P}^p(x)$ to form downstream states along the manifold. A shooting process is then applied to ensure successive points downstream satisfy constraints that enforce smoothness along the downstream manifold curve[6]. This process is then continued iteratively by shifting the working interval to the next set of computed manifold points downstream until a stopping condition is triggered: the manifold exits the domain of interest, the total length of the generated manifold surpasses a user-specified maximum arc length, or the generated manifold encounters another saddle point in the same island chain [6, 19].

Autonomous Topology Extraction Applied to Planar CR3BP Maps

As a sample application in a multi-body model, the automated fixed point detection portion of the automated topology algorithm is exercised on the domain D_{EM} in the Earth-Moon system. The orbit convolution image for $C = 2.96$ (Fig. 5) on this domain is incorporated to select the initial sampling grid as a 24×16 set of cells where each cell seemingly surrounds an isolated fixed point. The initial sampling is computed with $n = 200$ map iterations to compute the available periods up to $p_{max} = 12$ per-node that appear in Fig. 7. Tracking the rotation in $\boldsymbol{\Delta}$ outputs 11 possible fixed point locations where ambiguities nearing 180° exist with $\|\boldsymbol{\Delta}\| < 1 \times 10^{-4}$. Poincaré index considerations yield an additional 58 fixed point guesses

resulting from a 20×20 sub-cell grid search after a non-zero index is returned. After the corrections process is applied, 50 fixed points are located and added to a graphical environment (appearing in Fig. 9). Note that the 50 computed fixed points are included without the duplication and symmetry filters described in Section 3 for a closer examination of algorithm output. These computed fixed points represent less than 10 orbits since many of the solutions are duplicated at higher periods (e.g., the algorithm finds a period-1, period-9, and period-10 center all at the same location even though the true orbit is period-1). Most of the computed center points (green dots) reside in the middle of quasi-periodic regions appearing in the orbit convolution image, but a period-8 center island chain is also detected on the $x < 0$ side of the Earth. Saddle points are also detected and displayed as red dots in Fig. 9. Some of the saddle-type fixed points sit on visible structures in the orbit convolution image where an extension of gray persists into the chaotic sea; these fixed points likely correlate to an intersection of stable and unstable manifolds from low-period orbits which form higher-period fixed points [8, 11]. Overall, the fixed points in Fig. 9 present a good example of isolating orbital structures that exist in the chaos that is quite difficult to detect through the visual inspection of a puncture plot.

Sample orbits resulting from the autonomous extraction procedure in the Earth-Moon application are highlighted for further analysis. A set of center-type and saddle-type orbits are indicated on the Poincaré section in Fig. 9 along with the corresponding order of returns. The selected set is also plotted in configuration space (Fig. 10) with the same color-coding displayed in Fig. 9. State and period information about the set of orbits is tabulated in Table 1. The sample center points, labeled $C0$ (black), $C1$ (orange), and $C2$ (green), surround a particular primary with perpendicular crossings of Σ; these center orbits are also well-known with various applications to date [4, 5, 21]. Conversely, the resulting saddle-type orbits – $S0$ (red), $S1$ (blue), and $S2$ (purple) – exhibit complex behavior and may prove difficult to compute by
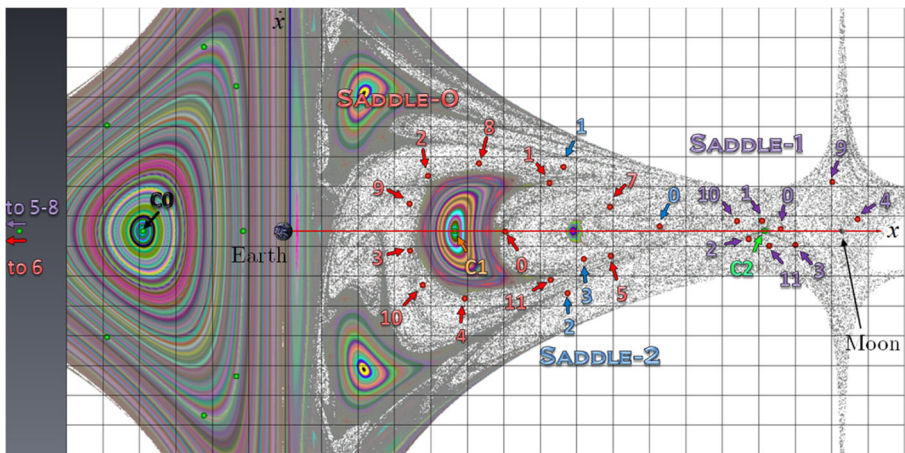
Fig. 9 Fixed points (*green* for centers and *red* for saddles) for the domain D_{EM} computed with the automated topology extraction procedure employing a 24×16 initial sampling grid and $n = 200$ initial map iterations ($p_{max} = 12$)
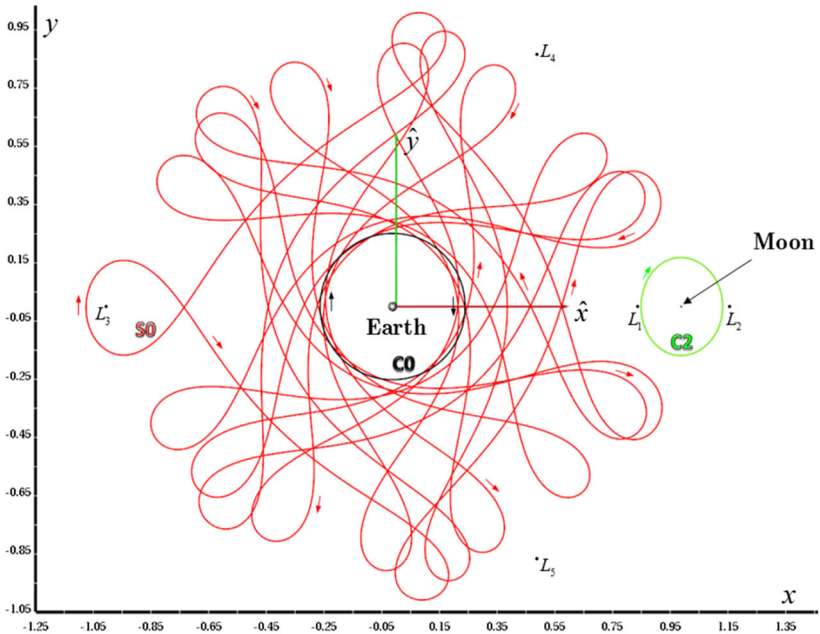
(a) Orbits $C0$, $C2$, and $S0$
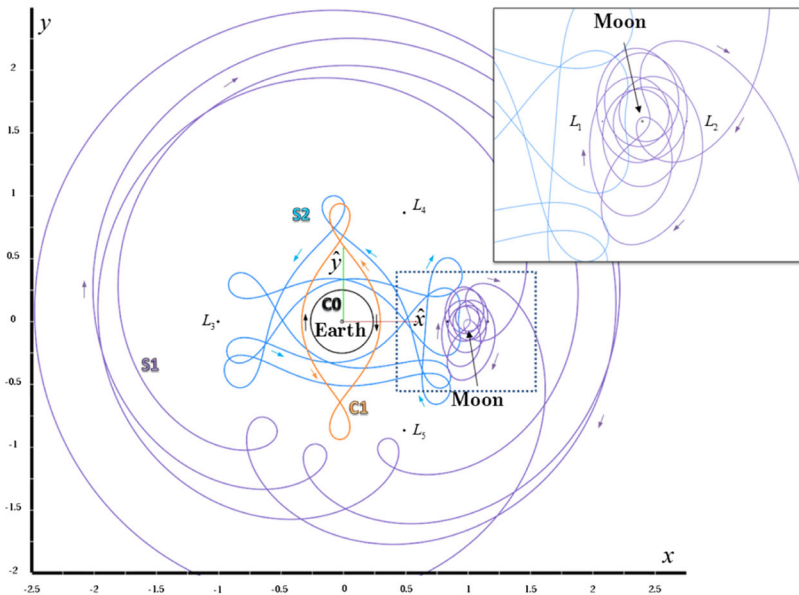
(b) Orbits $C0$, $C1$, $S1$, and $S2$

Fig. 10 Fixed points (*green* for centers and *red* for saddles) for the domain D_{EM} computed with the automated topology extraction procedure employing a 24×16 initial sampling grid and $n = 200$ initial map iterations ($C = 2.96$, $p_{max} = 12$)

Table 1 A sample of Earth-Moon periodic orbit initial state components on Σ resulting from the autonomous Poincaré map topology extraction algorithm employing a 24×16 initial sampling grid and $n = 200$ initial map iterations ($C = 2.96$, $p_{max} = 12$)

Orbit	p	Color	x (NonDim)	$\dot{x}$ (NonDim)	T (days)
$C0$	1	black	-0.263491972891	0.0	3.069
$C1$	1	orange	0.294802707935	0.0	27.112
$C2$	1	green	0.849016264023	0.0	10.065
$S0$	12	red	0.384994915649	-0.006895701932	326.099
$S1$	12	purple	0.878157738325	0.023107692739	295.432
$S2$	4	blue	0.661494496067	0.051881260690	135.003

Note, the given state corresponds to the crossing indicated by the number 0 in Fig. 9

conventional procedures, e.g., bifurcations from known orbit families (see Doedel et. al [5]). The autonomous topology extraction method, therefore, supplies new options for design in mutli-body regimes. For example, orbit $S1$ behaves in a manner similar to orbit $C2$ with returns near $C2$, but a pair of close lunar approaches transition orbit $S1$ from the lunar vicinity to and from an exterior orbit region surrounding the primary bodies. The stable and unstable manifolds of orbit $S1$ could be employed to seed initial guesses for capture or departure trajectories from the quasi-periodic region around orbit $C2$ [7, 21]. Thus, autonomous detection and extraction of fixed points on arbitrary sections may supply insight for orbital transfer design.

Although automated fixed point extraction offers access to some fixed points in the domain of interest, the orbit convolution image in Fig. 9 clearly reveals that numerous orbital structures are not captured due to various factors. One issue, in particular, is the size of the analysis cells. The grid cells may span too much space, thereby encapsulating a larger variety of local behavior. Note that the Poincaré index for a closed curve that encircles several fixed points is actually the sum of all the indexes around isolated fixed points[17]. Thus, if a cell surrounds multiple fixed points, the resulting Poincaré index might be zero even though fixed points exist inside the cell. Also, analysis cells with an invalid corner (or a corner residing in the forbidden region) are dismissed before analysis is initiated; however, many of these areas contain rich dynamical variance such as the chaotic regions in close proximity of the Moon as indicated in Fig. 9. Selecting a more refined grid, one that is isolated around a target region, will likely allow additional structures to emerge. Reducing the grid size too much, though, creates redundant analyses, especially in the large quasi-periodic regions.

Missing structure can also be attributed to the difficulty in tracking the displacement vector rotation along the boundary of a cell. Two phenomena present in the modeling formulation contribute to the discontinuities in tracking $\boldsymbol{\Delta}$ around a closed curve – highly sensitive dynamics that are known to exist in the CR3BP and the definition of Σ in relation to the dynamical flow. To demonstrate these issues, the orientation of $\boldsymbol{\Delta}$ for $p = 1$ is computed throughout a sample cell from Fig. 9 in a 20×20 sub-grid and is displayed in Fig. 11 with 256 divisions per-edge. The color in Fig. 11a displays the nondimensional magnitude of the map displacement vector according to the attached colorbar. This sample cell spans the $(x, \dot{x})$ nondimensional
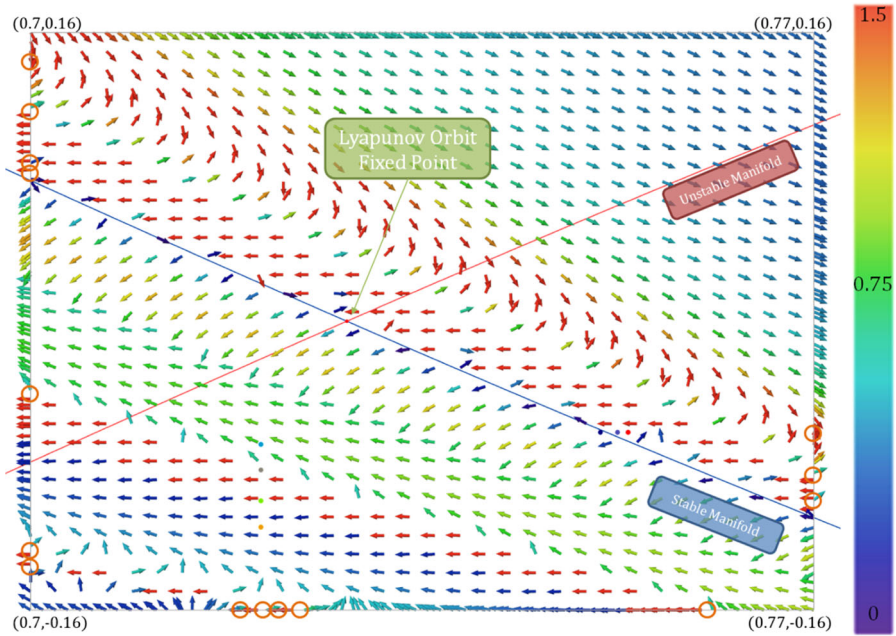
(a) Poincaré map displacement (colored by $\|\Delta\|$) for $p = 1$
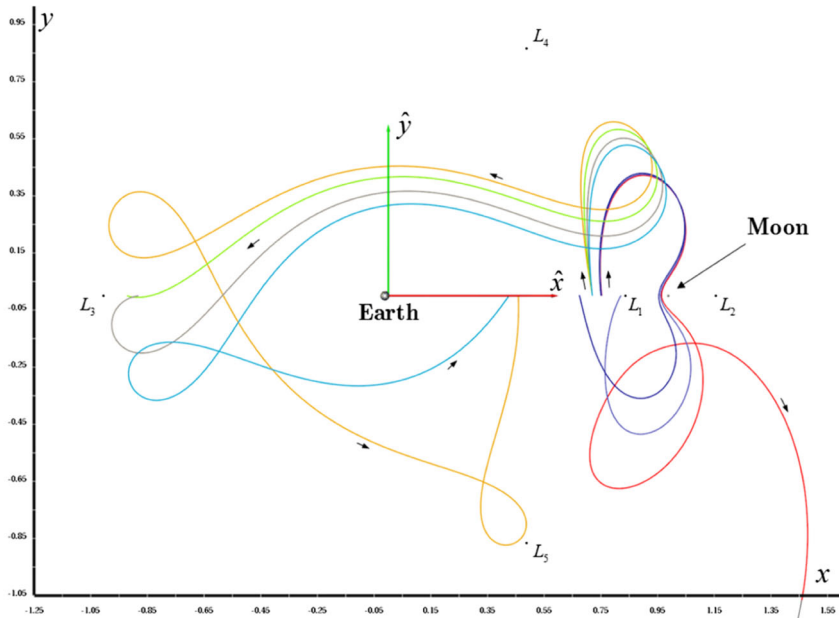
(b) Trajectories for $p = 1$ from sample points with similar color

Fig. 11 The orientation of the map displacement vector Δ evaluated with $p = 1$ for the cell ($x \in [0.7, 0.77]$, $\dot{x} \in [-0.16, 0.16]$) which encircles the L_1 Lyapunov orbit fixed point at $C = 2.96$ in the Earth-Moon system. Regions of ambiguous rotation in Δ along an edge are circled in orange

coordinates $(0.7, -0.16)$ to $(0.77, 0.16)$) and encircles the period-1 fixed point representing the Lyapunov orbit about the Lagrange point L_1 (at roughly $(0.728, 0.0)$). The depiction of the orientation of the various $\boldsymbol{\Delta}$ vectors (Fig. 11) clearly conveys that $\boldsymbol{\Delta}$ can flip direction readily along edges. Locations along an edge for which the rotation is not resolved utilizing a $d_{min} = 0.32/256$, or 256 divisions along the smaller dimension, are highlighted by orange circles in Fig. 11. Some orange circles occur where the nearby $\|\boldsymbol{\Delta}\|$ values are similar (color in Fig. 11a) but the orientation flips between nearby starting locations. Such behavior correlates with a propagation through a singularity such as the Moon in this example. Perhaps more prevalent are locations in this sample cell where $\|\boldsymbol{\Delta}\|$ is discontinuous. Discontinuities in $\|\boldsymbol{\Delta}\|$ are examined by computing $p = 1$ trajectories in affected areas with the colored points in Fig. 11a and corresponding trajectories displayed in Fig. 11b. Since the trajectories in Fig. 11b possess returns to Σ on opposite sides of the Earth, these sample trajectories suggest that the hyperplane $\Sigma : y = 0$ is not truly transverse to the flow everywhere within this cell. Such behavior violates a fundamental definition of a Poincaré section, rendering some ambiguity in the computation of the $\boldsymbol{\Delta}$ rotation. With the multitude of unresolved rotations, this cell is forced to be tagged as one with no Poincaré index for $p = 1$ by the algorithm, even though a fixed point is known to exist within this cell. Resolving the rotation of the vector $\boldsymbol{\Delta}$ remains an open issue and is currently under investigation.

The fixed point extraction process is also applied to the Jupiter-Europa system within the specified domain D_{JE}. Examining the orbit convolution image for D_{JE} in Fig. 4b, a 20×20 grid spanning D_{JE} appears appropriate for isolating possible fixed points inside a single cell. The parameters $n = 200$ and $p_{max} = 12$ are again employed to generate possible toroidal periods per-node. The resulting fixed points from the automated extraction process are visualized with the orbit convolution image in Fig. 12, where green and red dots correspond to center-type and saddle-type orbits, respectively. As evident from Fig. 12, more fixed points are located with automated detection in this Jupiter-Europa domain than in the Earth-Moon domain. The enhancement in the quantity of fixed points is attributed to a reduced sensitivity in resolving the rotation of map displacement ($\boldsymbol{\Delta}$) in the Jupiter-Europa example since Poincaré section singularities (e.g., at the Earth and Moon in D_{EM}) are not present in this particular domain. Clearly, saddle points exist throughout the chaotic (gray) regions; however, fixed points that should appear as centers when examining the orbit convolution image are mistakenly classified as saddles due to numerical difficulties when computing the eigenvalues of the monodromy matrix[13]. Many high-period fixed points are excited in this region, including several island chains that exist around a period-1 center. The application of automated fixed point detection to D_{JE} demonstrates that there is a wealth of structure residing in the chaos that may be difficult to recognize otherwise.

The next step in the topology extraction process is the computation of the invariant manifolds emanating from the saddle points. Applying the global continuation method for 1D manifolds, though, is quite challenging in the planar CR3BP. Manifolds corresponding to the Earth-Moon Lyapunov orbit about the L_1 Lagrange point are computed as an application of the global continuation scheme for 1D manifolds. The resulting curves possess a continuous and dense (thousands of states on the map)
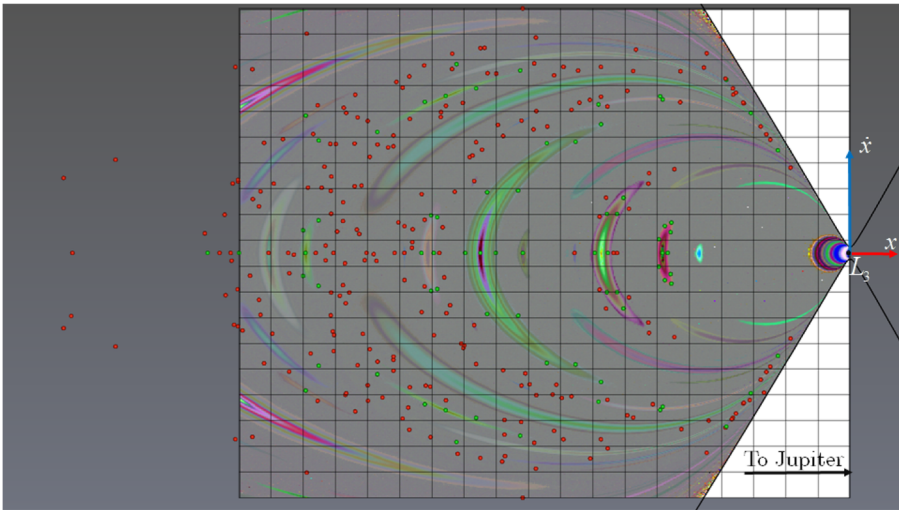
Fig. 12 Fixed points for the domain D_{JE} computed with the automated topology extraction procedure employing a 20×20 initial sampling grid and $n = 200$ initial map iterations ($p_{max} = 12$)

representation of the stable and unstable manifolds associated with the saddle point as is apparent in Fig. 13. The termination of the continuation process, however, is triggered by either sharp turns of the true manifolds on the Poincaré section, e.g., near the zero-velocity curves, or because manifolds become tangent to Σ and transition to a new area on the Poincaré section (similar to flow behavior presented in Fig. 11b).
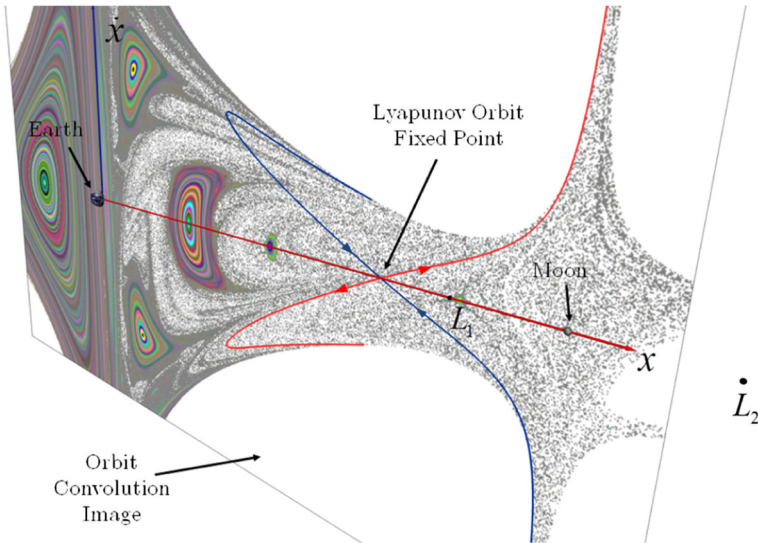
Fig. 13 A visual design environment displaying an orbit convolution visualization for the Earth-Moon system combined with the stable (blue) and unstable (red) manifolds of the L_1 Lyapunov orbit computed with the manifold computation algorithm summarized by England et al. [6]

The manifolds do not truly possess a discontinuity as the space is area-preserving [8, 11], but numerically following the manifold through a singularity in the dynamical model (such as a primary) or a "jump" in section-space coordinates is exceptionally difficult. Employing an effective method to incorporate these issues into a manifold propagation algorithm warrants further study.

Concluding Remarks

Enhancing Poincaré map visualization beyond the *de facto* puncture plot generates a new view of the structures that exist on a surface of section in astrodynamics problems. The application of orbit convolution imagery demonstrates a clear contrast between quasi-periodic and ergodic behavior and supplies essential input for an automated topology extraction process. Employing a set of winding numbers to classify behavior throughout a domain and a numerical application of the Poincaré index enables the independent production of fixed points. Thus, computing periodic orbits on a Poincaré surface of section is attainable without significant external input from a trajectory designer.

Although this investigation introduces a framework for automated Poincaré map topology extraction, many components of the algorithm could benefit with further development. Defining an optimal cell size for analysis or an adaptive refinement procedure could offer an intelligent way to focus analysis where dynamically rich information resides. Another possible adaptation involves a new definition or modification of a hyperplane such that the Poincaré section is universally transverse to the flow, significantly improving the detection of fixed points within analysis cells. In addition, locating initial guesses closer to the true fixed points and a more robust differential corrections scheme would enhance the fixed point computation process. Finally, the manifold computation method should smooth discontinuities in manifolds on arbitrary hyperplanes. With such upgrades, the algorithm would provide a more in-depth view of the topological construct available throughout any arbitrary Poincaré section.

An automated approach for exposing the interconnectivity of orbital structures facilitates spacecraft trajectory design with a broad range of options without external computation. When implemented in a visual environment, a designer can employ automated topological skeletons to select pathways that navigate the available dynamical flow. By selecting stable and unstable manifolds corresponding to various fixed points that are available on a Poincaré map, low-cost transfers can potentially be traced through the stable-unstable manifold connections since all of the relevant orbital data is automatically generated as part of the process. Such a visually interactive tool could expedite the generation of tour designs as well as assist in the design of multi-body orbital structures.

Multivariate Fields for Scalable Visualizations. This effort is also supported by the Computer Science Department and the School of Aeronautics and Astronautics at Purdue University.

References

1. Anderson, R.L., Lo, M.W.: A dynamical systems analysis of resonant flybys: Ballistic case. J. Astronaut. Sci. **58**(2), 167–194 (2011)
2. Cabral, B., Leedom, L.C.: Imaging Vector Fields Using Line Integral Convolution, pp. 263–270. ACM, New York, NY, USA (1993)
3. Danby, J.M. Fundamentals of Celestial Mechanics, 2nd edn. Willmann-Bell, Inc., Richmond, Virginia (1992)
4. Demeyer, J., Gurfil, P.: Transfer to distant retrograde orbits using manifold theory. J. Guid. Control Dyn. **30**, 5 (2007)
5. Doedel, E.J., Romanov, V.A., Paffenroth, R.C., Keller, H.B., Dichmann, D.J., Galan-Vioque, J., Vanderbauwhede, A.: Elemental periodic orbits associated with the libration points in the circular restricted 3-body problem. Int. J. Bifurcation Chaos **17**(8), 2625–2677 (2007)
6. England, J., Krauskopf, B., Osinga, H.: Computing one-dimensional global manifolds of Poincaré maps by continuation. SIAM J. Appl. Dyn. Syst. **4**(4), 1008–1041 (2005)
7. Gómez, G., Koon, W.S., Lo, M.W., Marsden, J.E., Masdemont, J., Ross, S.D.: Connecting orbits and invariant manifolds in the spatial restricted three-body problem. Nonlinearity **17**, 1571–1606 (2004)
8. Guckenheimer, J., Holmes, P.: Nonlinear Oscillations, Dynamical Systems, and Bifurcations of Vector Fields. Springer-Verlag, New York. New York (1983)
9. Haapala, A., Howell, K.C.: Trajectory design strategies applied to temporary comet capture including Poincaré maps and invariant manifolds. Celest. Mech. Dyn. Astron. **116**(3), 299–323 (2013)
10. Koon, W.S., Lo, M.W., Marsden, J.E., Ross, S.D.: Heteroclinic connections between periodic orbits and resonance transitions in celestial mechanics. Chaos **10**(2), 427–469 (2000)
11. Lichtenberg, A.J., Lieberman, M.A. Regular and Chaotic Dynamics, 2nd edn. Springer-Verlag, New York, New York (1992)
12. Lo, M.W., Anderson, R.L., Lam, T., Whiffen, G.: The role of invariant manifolds in low thrust trajectory design (Part III). In: AAS/AIAA Spaceflight Dynamics Conference. Tampa, Florida. Paper AAS 06-190 (2006)
13. Press, W.H., Teukolsky, S.A., Vetterling, W.T., Flannery, B.P. Numerical Recipes: The Art of Scientific Computing, 3rd edn. Cambridge University Press, New York (2007)
14. Sanderson, A.R., Chen, G., Tricoche, X., Pugmire, D., Kruger, S., Breslau, J.: Analysis of recurrent patterns in toroidal magnetic fields. In: Visualization Information Visualization 2010, IEEE Transactions on Visualization and Computer Graphics, vol. 16 (2010)
15. Schlei, W.: An Application of Visual Analytics to Spacecraft Trajectory Design. M.S. Thesis, School of Aeronautics and Astronautics, Purdue University. West Lafayette, Indiana (2011)
16. Shoemake, K.: Rational approximation. In: Paeth, A.W. (ed.) Graphics Gems V, vol. 25–32. Academic Press, San Diego (1995)
17. Strogatz, S.H.: Nonlinear Dynamics and Chaos. Westview Press, Perseus Books Publishing, Cambridge (1994)
18. Thrill, M.: A more precise rounding algorithm for rational numbers. Computing **82**(2–3), 189–198 (2008)
19. Tricoche, X., Garth, C., Sanderson, A.: Visualization of topological structures in area-preserving maps. IEEE Trans. Vis. Comput. Graph. **17**(12), 1765–1774 (2011)
20. Vaquero, M., Howell, K.C.: Leveraging resonant orbit manifolds to design transfers between libration point orbits in multi-body regimes. In: 23rd AAS/AIAA Space Flight Mechanics Meeting Kauai Hawaii (2013)
21. Vaquero, M., Howell, K.C.: Transfer design exploiting resonant orbits and manifolds in the saturn-titan system. J. Spacecr. Rocket. **50**(5), 1069–1085 (2013)
22. Villac, B.F., Scheeres, D.J.: Escaping trajectories in the hill three-body problem and applications. J.Guid. Control, Dyn. **26**(2), 224–232 (2003)
23. Yip, K.M.K.: KAM: A System for Intelligently Guiding Numerical Experimentation by Computer. The MIT Press (1991)